Weierstraß-Institut
für Angewandte Analysis und Stochastik

Leibniz-Institut im Forschungsverbund Berlin e. V.

Preprint ISSN 2198-5855

Modeling and simulation of the lateral photovoltage scanning method

Patricio Farrell[1], Stefan Kayser[1], Nella Rotundo[2]

submitted: October 29, 2020

[1] Weierstrass Institute
Mohrenstr. 39
10117 Berlin
Germany
E-Mail: patricio.farrell@wias-berlin.de
stefan.kayser@wias-berlin.de

[2] University of Florence
Department of Mathematics and Computer Science
"Ulisse Dini" (DIMAI)
Viale Morgagni 67 A
50134 Florence
Italy
E-Mail: nella.rotundo@unifi.it

No. 2784
Berlin 2020

2010 *Mathematics Subject Classification.* 35Q81, 35K57, 65N08.

Key words and phrases. Lateral-photovoltage-scanning method (LPS), semiconductor simulation, van Roosbroeck system, finite volume simulation, crystal growth.

The authors would like to thank Natasha Dropka, Jürgen Fuhrmann, Timo Streckenbach and Hang Si for their valuable input. The temperature field simulation in Figure 1 are courtesy of Robert Menzel (Leibniz-Institut für Kristallzüchtung). We thank the Deutsche Forschungsgemeinschaft (DFG) under Germany's Excellence Strategy EXC2046: MATH+ for funding the project IN-B3 (S.K.).

Edited by
Weierstraß-Institut für Angewandte Analysis und Stochastik (WIAS)
Leibniz-Institut im Forschungsverbund Berlin e. V.
Mohrenstraße 39
10117 Berlin
Germany

Fax: +49 30 20372-303
E-Mail: preprint@wias-berlin.de
World Wide Web: http://www.wias-berlin.de/

Modeling and simulation of the lateral photovoltage scanning method

Patricio Farrell, Stefan Kayser, Nella Rotundo

Abstract

The fast, cheap and nondestructive lateral photovoltage scanning (LPS) method detects inhomogeneities in semiconductors crystals. The goal of this paper is to model and simulate this technique for a given doping profile. Our model is based on the semiconductor device equations combined with a nonlinear boundary condition, modelling a volt meter. To validate our 2D and 3D finite volume simulations, we use theory developed by Tauc [22] to derive three analytical predictions which our simulation results corroborate, even for anisotropic 2D and 3D meshes. Our code runs about two orders of magnitudes faster than earlier implementations based on commercial software [14]. It also performs well for small doping concentrations which previously could not be simulated at all due to numerical instabilities. Our simulations provide experimentalists with reference laser powers for which meaningful voltages can still be measured. For higher laser power the screening effect does not allow this anymore.

1 Introduction

Semiconductor crystals are the very basis for any optoelectronic component such as transistors, LEDs or solar cells. Crystals are solid substances with an inherent structure/symmetry. To grow these crystals, amorphous crystalline material e.g. raw silicon is heated until it melts. As it cools down, the atoms are forced to build bonds. During solidification a seed crystal may enforce a preferred crystallization direction in these bonds, creating a single crystal. Two well-established single crystal growth techniques dominate the market. On the one hand, Czochralski grown crystals (95% market share) are cheap to produce but systematically introduce oxygen and carbon into the crystal, thus limiting their quality severely [24]. On the other hand, floating zone crystals (5% market share) produce purer crystals, however, severely increase the production cost [4].

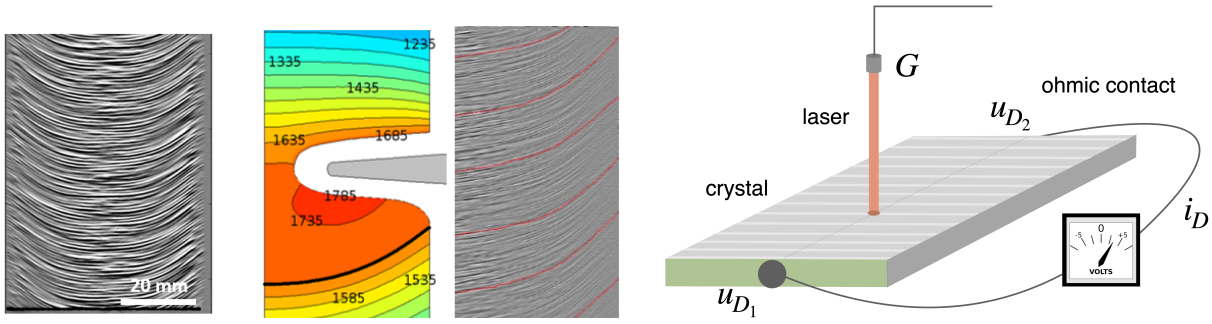

Figure 1: Striations from LPS measurement (left); temperature field simulation created by a coil (the black line represents the solid-liquid interface at $1687\,\mathrm{K}$) as well the corresponding striations (middle); LPS measurement setup (right).

In order to improve the crystal growth design, it is crucial to predict the temperature distribution of the coils which heat up the raw material. Unfortunately, it is impossible to measure the temperature distribution inside of the growing crystal during the production process. Silicon, for example, melts

DOI 10.20347/WIAS.PREPRINT.2784 Berlin 2020

at $1687\,\mathrm{K}$. However, along the solid-liquid interface microscopic variations in the crystal appear, see Figure 1 (left and middle). These so-called *striations* can be measured even in the cooled-down crystal. Traditionally, the local doping concentration is measured by analyzing the electric resistivity of the crystal [23]. The main drawbacks of this technique are the relatively poor spatial resolution (few millimeters) and the long acquisition time. Another technique is *secondary ion mass spectroscopy* (SIMS). Unfortunately, it is intrinsically destructive and detects only high doping concentrations $N_A > 1 \times 10^{15}\,\mathrm{cm}^{-3}$ for light elements such as boron [7].

To overcome all these limitations, the *lateral photovoltage scanning* method (LPS) has been proposed [19]. This opto-electrical measurement procedure detects doping inhomogeneities at wafer-scale and room temperature in a non-destructive fashion, see Figure 1 (right). Interestingly, besides being very cost-effective and fast, this tabletop setup is especially suitable for low doping concentrations ($10^{12}\,\mathrm{cm}^{-3}$ to $10^{16}\,\mathrm{cm}^{-3}$) and thus applies to a larger range of doping concentrations than SIMS. The LPS method excites the semiconductor crystal with a laser, creating a voltage difference at the sample edges which is proportional to the local doping variation. This voltage difference can be measured, from which one can infer the doping profile from the voltage difference. However, from a mathematical point of view one has to solve an inverse problem. An efficient solution of this inverse problem – an ambitious future task – requires a fast and reliable solution of the *forward* problem (where the voltage difference is determined from a nonlinear boundary condition).

For this reason we derive a charge transport model of the LPS measurement setup. With the help of our model we then simulate the forward model of the LPS measurement technique. To check the validity of our simulation results, we use theoretical observations proposed by Tauc in the 1950ies [22]. From his theory we derive three analytical predictions: First, the LPS voltage depends on local doping variations at least for low laser powers. Second, eventually the LPS voltage saturates for higher laser intensities due to the screening effect. And third, the LPS voltage depends logarithmically on moderate laser intensities. All three predictions are verified by our simulations and even hold true for anisotropic 2D and 3D meshes.

Our simulations rely on a Voronoi finite volume discretization which has been presented in [11, 10, 17]. The flux discretization is handled by ideas of Scharfetter and Gummel [20]. So far it seems only one implementation of the forward LPS method exists by Kayser et al. [16, 14] based on commercial software. Our open-source code reduces the simulation time by two orders of magnitude. This is crucial since a future aim is to efficiently solve the corresponding inverse problem. Moreover, our method presented here also works well for very low doping concentrations which previously could not be simulated due to numerical instabilities [16, 14]. We implement the nonlinear LPS boundary condition via the secant method. We also present a convergence study which shows that the LPS voltage converges quadratically. Finally, we provide experimentalists with reference laser powers for which meaningful voltages can still be measured. For higher laser power the screening effect does not allow this anymore.

To the best of our knowledge, the LPS technique has not been studied mathematically. Related (inverse) models for laser beam and electron induced current (LBIC and EBIC) exist. Simplified models have been studied in [6, 5, 18]. For these models, the setup the contacts are located in different areas and a current is measured instead of a voltage. The analytical theory behind coupling charge transport with circuits is addressed for example in [2, 3] and in the references therein.

The remainder of the paper is organized as follows: In the following section, we introduce the LPS model and Tauc' theory. In particular we describe the nonlinear boundary condition that models the voltage meter. In the following sections, we then describe the finite volume discretization, present our simulation results and conclude.

2 LPS model

In this section, we describe first the charge transport model, then the circuit model which describes the LPS measurement technique.

2.1 The van Roosbroeck model

We model the silicon crystal as a bounded domain $\Omega \subset \mathbb{R}^3$. Its doping profile is given by the difference of donor and acceptor concentrations, $N_D(\mathbf{x}) - N_A(\mathbf{x})$, where $\mathbf{x} = (x, y, z)^T \in \Omega$.

Within the crystal we consider two charge carriers: Electrons with negative elementary charge $-q$, and holes with positive elementary charge q. The charge transport within the crystal is described in terms of the electrostatic potential, denoted by $\psi(\mathbf{x})$, and quasi Fermi potentials for electron and holes, denoted by $\varphi_n(\mathbf{x})$ and $\varphi_p(\mathbf{x})$. The current densities for electrons and holes are given by $\boldsymbol{J}_n(\mathbf{x})$, $\boldsymbol{J}_p(\mathbf{x})$. These variables satisfy the following steady-state system, the so-called van Roosbroeck model,

$$\begin{aligned} -\nabla \cdot (\varepsilon \nabla \psi) &= q(p(\psi, \varphi_p) - n(\psi, \varphi_n) + N_D(\mathbf{x}) - N_A(\mathbf{x})) \\ -\frac{1}{q} \nabla \cdot \boldsymbol{J}_n &= G(\mathbf{x}) - R(\psi, \varphi_n, \varphi_p), \qquad \boldsymbol{J}_n = -q\mu_n n(\psi, \varphi_n) \nabla \varphi_n, \\ \frac{1}{q} \nabla \cdot \boldsymbol{J}_p &= G(\mathbf{x}) - R(\psi, \varphi_n, \varphi_p), \qquad \boldsymbol{J}_p = -q\mu_p p(\psi, \varphi_p) \nabla \varphi_p. \end{aligned} \tag{1}$$

The first equation is a nonlinear Poisson equation, describing a self-consistent electric field. The following two continuity equations describe the charge transport in the crystal.

Assuming so-called Boltzmann statistics, the relations between the quasi-Fermi potentials and the densities of electrons and holes, n and p respectively, are given by

$$n(\psi, \varphi_n) = N_c \exp\left(\frac{q(\psi - \varphi_n) - E_c}{k_B T}\right) \qquad \text{and} \qquad p(\psi, \varphi_p) = N_v \exp\left(\frac{q(\varphi_p - \psi) + E_v}{k_B T}\right). \tag{2}$$

Here, we have denoted the conduction and valence band densities of states with N_c and N_v, the Boltzmann constant with k_B and the temperature with T. Furthermore, E_c and E_v refer to the constant conduction and valence band-edge energies, respectively. Using the relations (2) the current densities can be written in the following drift-diffusion form

$$\boldsymbol{J}_n = -q\mu_n(n\nabla\psi - U_T \nabla n), \qquad \boldsymbol{J}_p = -q\mu_p(p\nabla\psi + U_T \nabla p),$$

in which $U_T = k_B T/q$ is the thermal voltage. The intrinsic carrier density n_i is defined via the relationship

$$n_i^2 = N_c N_v \exp\left(-\frac{E_c - E_v}{k_B T}\right). \tag{3}$$

If we neglect both transport equations, and only solve the nonlinear Poisson equation in (1) for the electrostatic potential ψ_{eq} and fixed quasi Fermi potentials $\varphi_n = \varphi_p = 0$, we say that the semiconductor is in *equilibrium*. The corresponding equilibrium charge densities n_{eq} and p_{eq} satisfy

$$n_{eq} p_{eq} = n_i^2. \tag{4}$$

The precise geometry Ω will be specified in the following Section 2.6.

2.2 Boundary conditions

The stationary van Roosbroeck system (1) is usually supplied with Dirichlet-Neumann boundary conditions. We assume that the boundary $\partial\Omega$ is the union of two disjoint parts Γ_N and Γ_D. On Γ_N, we assign Neumann boundary conditions

$$\frac{\partial\psi}{\partial\boldsymbol{\nu}} = \frac{\partial\varphi_n}{\partial\boldsymbol{\nu}} = \frac{\partial\varphi_p}{\partial\boldsymbol{\nu}} = 0, \tag{5}$$

where $\partial/\partial\boldsymbol{\nu} = \boldsymbol{\nu}\cdot\nabla$ is the normal derivative along the external unit normal $\boldsymbol{\nu}$.

On Γ_D, we assign Dirichlet-type boundary conditions. This type of boundary condition models so-called ohmic contacts. We suppose that there are two ohmic contacts, i. e. $\Gamma_D = \Gamma_{D_1} \cup \Gamma_{D_2}$. The ohmic boundary conditions can be summarized by

$$\psi - \psi_0 = \varphi_n = \varphi_p = u_{D_i} - u_{\text{ref}} \quad \text{on} \quad \Gamma_{D_i}, \quad i = 1, 2, \tag{6}$$

where ψ_0 is the local electroneutral potential which one obtains by solving the Poisson equation for ψ for a vanishing left-hand side. The terms u_{D_i} denote the contact voltages at the corresponding ohmic contacts. It is common to define a reference value u_{ref} of the potential. We set $u_{\text{ref}} = 0$.

The electric current j_{D_i} flowing through the i-th ohmic contact Γ_{D_i} is defined by the surface integral

$$j_{D_i} = -\int_{\Gamma_{D_i}} \boldsymbol{\nu}\cdot(\boldsymbol{J}_n(\mathbf{x}) + \boldsymbol{J}_p(\mathbf{x}))d\sigma(\mathbf{x}), \qquad i = 1, 2. \tag{7}$$

According to the conservation of charge, the currents in (7) satisfy the relation $\sum_{i=1}^{2} j_{D_i} = 0$. For notational convenience we define

$$i_D := j_{D_1} = -j_{D_2}. \tag{8}$$

2.3 Arora mobility model

The Arora mobility model takes into account the scattering of charge carriers with ionized impurities, most likely by doping. The electron and hole mobilities are given by

$$\mu_n = \mu_{n,\min} + \frac{\mu_{n,0}}{1 + \left(\frac{N_D+N_A}{N_{D0}}\right)^{\alpha_n}} \qquad \text{and} \qquad \mu_p = \mu_{p,\min} + \frac{\mu_{p,0}}{1 + \left(\frac{N_D+N_A}{N_{A0}}\right)^{\alpha_p}}, \tag{9}$$

where the different parameters are given by

$$\begin{aligned}
\mu_{n,\min} &= \mu_{n,\min}^{\text{ref}} \cdot \left(\frac{T_0}{300\,\text{K}}\right)^{\beta_1}, \quad \mu_{p,\min} = \mu_{p,\min}^{\text{ref}} \cdot \left(\frac{T_0}{300\,\text{K}}\right)^{\beta_1}, \\
\mu_{n,0} &= \mu_{n,0}^{\text{ref}} \cdot \left(\frac{T_0}{300\,\text{K}}\right)^{\beta_2}, \quad \mu_{p,0} = \mu_{p,0}^{\text{ref}} \cdot \left(\frac{T_0}{300\,\text{K}}\right)^{\beta_2}, \\
N_{D0} &= N_{D0}^{\text{ref}} \cdot \left(\frac{T_0}{300\,\text{K}}\right)^{\beta_3}, \quad N_{A0} = N_{A0}^{\text{ref}} \cdot \left(\frac{T_0}{300\,\text{K}}\right)^{\beta_3}, \\
\alpha_n &= \alpha_0 \cdot \left(\frac{T_0}{300\,\text{K}}\right)^{\beta_4}, \quad \alpha_p = \alpha_0 \cdot \left(\frac{T_0}{300\,\text{K}}\right)^{\beta_4}.
\end{aligned}$$

Again the remaining parameters are found in Appendix A.1.

2.4 Recombination rates

The total recombination rate is given by the sum of all recombination rates. We consider three recombination mechanisms,

$$R = R_{\mathsf{dir}} + R_{\mathsf{Aug}} + R_{\mathsf{SRH}}, \tag{10}$$

that is, the direct recombination

$$R_{\mathsf{dir}} = C_d(np - n_i^2) \tag{11}$$

the Auger recombination

$$R_{\mathsf{Aug}} = C_n n(np - n_i^2) + C_p p(np - n_i^2) \tag{12}$$

and the Shockley-Read-Hall recombination

$$R_{\mathsf{SRH}} = \frac{np - n_i^2}{\tau_p(n + n_T) + \tau_n(p + p_T)}. \tag{13}$$

In contrast to the robust Auger, the Shockley-Read-Hall (SRH) recombination will vary for different samples due to unintentional incorporation of elements which results into different life times τ_n, τ_p and reference densities n_T, p_T. The remaining parameters are collected in Appendix A.1.

2.5 Generation rate

When the laser hits the crystal, some photons are reflected with constant reflectivity $\mathcal{R}$. The other *impinged* photons create electron-hole pairs, resulting in a generation rate defined as follows

$$G(\mathbf{x}) = N_{ph}(1 - \mathcal{R})S(\mathbf{x}), \tag{14}$$

where $S(\mathbf{x})$ is the shape function of the laser (normalized by $\int_\Omega S(\mathbf{x})d\mathbf{x} = 1$) and N_{ph} the impinging photon rate on the whole surface of the sample given by

$$N_{ph} = \frac{P\lambda_L}{hc}. \tag{15}$$

Here, P denotes the laser power, λ_L the wave length of the laser and $hc = 6.6 \times 10^{-34}\,\mathrm{m^2kg/s} = 6.6 \times 10^{-34}\,\mathrm{Js}$ the Planck constant. The shape function S depends on the spatial dimension. Hence, we will specify it for each geometry separately.

2.6 Geometries and shape functions

We will consider 1D, 2D and 3D setups for the silicon crystal. Each sample has to be sufficiently larger than the mean free path of the electrons. The necessary length depends on the assumed charge carrier life times but it can reach millimeter scale. The active region is highly centralized. A fact that our meshes will need to respect. For large charge carrier life times (millisecond range) it might be necessary to increase the sample length. The height of the sample is directly related to the penetration depth of the laser. For a laser with wave length $\lambda = 685\,\mathrm{nm}$, the penetration depth is approximately 5 nm, and so $99.996\,\%$ of the laser energy is absorbed in the sample. For smaller laser wave lengths a sufficient amount of the laser energy is still absorbed.

2.6.1 1D model

For the one dimensional model, the domain is given by

$$\Omega = \{(x, y, z) \in \mathbb{R}^3 \mid x \in [-\ell/2, \ell/2], y = 0, z = 0\}$$

and the boundary consists of two points $\mathcal{W} = (-\ell/2, 0, 0)$ and $\mathcal{E} = (\ell/2, 0, 0)$ with $\ell = 3\,\text{mm}$. The geometry is shown in Figure 2 on the left. The 1D shape function in (14) is given by

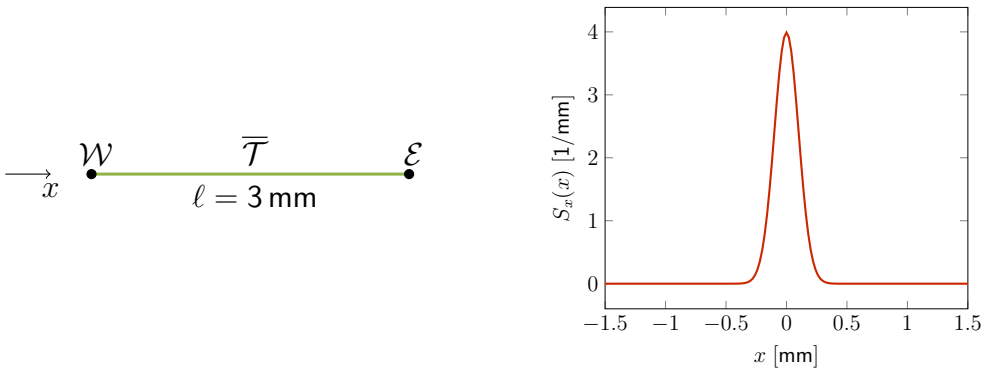

Figure 2: 1D model: geometry (left) and shape function (right)

$$S_x(x) = \frac{1}{\sqrt{2\pi}\sigma_{\text{L}}} \exp\left[-\frac{1}{2}\left(\frac{x - x_0}{\sigma_{\text{L}}}\right)^2\right], \tag{16}$$

where x_0 denotes the position of the laser and σ_L the laser spot radius, see the image on the right in Figure 2.

2.6.2 2D model

In the two dimensional case, the domain is the surface

$$\Omega = \{(x, y, z) \in \mathbb{R}^3 \mid x \in [-\ell/2, \ell/2], y = 0, z \in [-h, 0]\}.$$

with $\ell = 3$mm and height $h = 5 \times 10^{-5}$mm. It is visualized in Figure 3.

The 2D shape function in (14) is given by

$$S(x, z) = S_x(x) \cdot S_z(z)$$

where in z direction the absorption of the laser is assumed to be an exponential decay function

$$S_z(z) = \frac{1}{d_A} \exp\left[-\frac{|z|}{d_A}\right]. \tag{17}$$

Here d_A is the penetration depth, or in other words $1/d_A$ is the absorption coefficient, which heavily depends on the laser wave length. In x direction the one-dimensional Gaussian (16) from the previous section is used. The shape function in 2D is visualized in Figure 3 on the right.

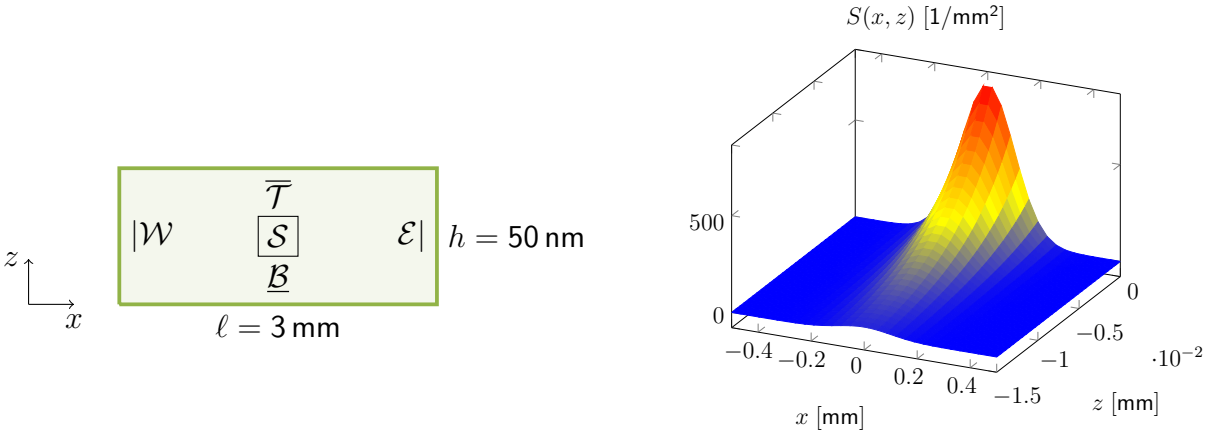

Figure 3: 2D model: geometry (left) and shape function (right)

2.6.3 3D model

The three-dimensional setup is a cuboid given by

$$\Omega = \{(x, y, z) \in \mathbb{R}^3 \mid x \in [-\ell/2, \ell/2], y \in [0, w], z \in [-h, 0]\}$$

with length $\ell = 3$mm, width $w = 0.5$mm and height $h = 5 \times 10^{-5}$mm, see Figure 4. The boundary of the domain $\partial\Omega$ consists of six surfaces, defined by

$$\begin{aligned} \mathcal{W} &= \Omega \cap \{(x, y, z) \in \mathbb{R} \mid x = -\ell/2\}, & \mathcal{E} &= \Omega \cap \{(x, y, z) \in \mathbb{R} \mid x = \ell/2\}, \\ \mathcal{S} &= \Omega \cap \{(x, y, z) \in \mathbb{R} \mid y = 0\}, & \mathcal{N} &= \Omega \cap \{(x, y, z) \in \mathbb{R} \mid y = w\}, \\ \mathcal{T} &= \Omega \cap \{(x, y, z) \in \mathbb{R} \mid z = 0\}, & \mathcal{B} &= \Omega \cap \{(x, y, z) \in \mathbb{R} \mid z = -h\}. \end{aligned}$$

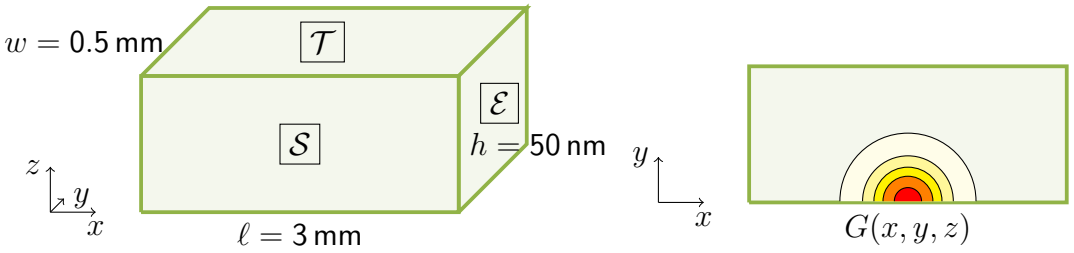

Figure 4: 3D model: geometry (left) and shape function (right)

The 3D shape function in (14) is given by

$$S(x, y, z) = S_{xy}(x, y) \cdot S_z(z).$$

In z direction the absorption of the laser is again assumed to be the exponential decay function (17). For $S_{xy}(x, y)$ a two dimensional Gaussian distribution is assumed:

$$S_{xy}(x, y) = S_x(x) S_y(y) = \frac{1}{2\pi\sigma_L^2} \exp\left[-\frac{1}{2}\left(\frac{x - x_0}{\sigma_L}\right)^2\right] \exp\left[-\frac{1}{2}\left(\frac{y - y_0}{\sigma_L}\right)^2\right]. \tag{18}$$

That is, the laser hits the crystal at $(x_0, y_0, 0)^T$. A contour plot of the xy plane is shown in Figure 4 on the right.

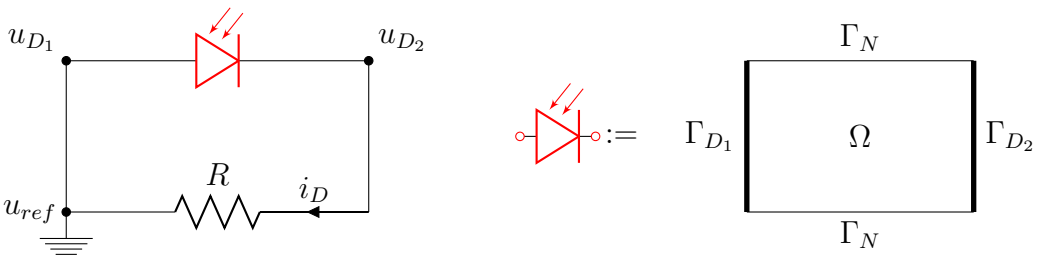

Figure 5: On the left we show a sample of photo-sensitive silicon crystal (in red) coupled with the voltage meter having resistance $\mathcal{R}$. On the right, we show the domain Ω and the ohmic contacts Γ_{D_1} and Γ_{D_2}.

2.7 Coupling the device to an external circuit

So far we have described the van Roosbroeck system. It models charge transport in semiconductors but not the LPS setup itself. To achieve the latter, we model the voltage meter as a simple circuit having a resistance $\mathcal{R}$. This structure is visualized in Figure 2.7. The network has two nodes, in which the potentials are respectively u_{D_1} and u_{D_2}. Using the formalism of the Modified Nodal Analysis (MNA) we have that the difference between the electric potentials at the nodes is given by

$$u_{D_2} + \psi_0|_{\Gamma_{D_2}} - (u_{D_1} + \psi_0|_{\Gamma_{D_1}}) = \mathcal{R}\, i_D(u_{D_2}), \tag{19}$$

where i_D is defined in (8). Usually one of the nodes of an electric circuit is assumed to have an electric potential equal to the ground. This means in our case that we can arbitrarily set $u_{D_1} = u_{\text{ref}} = 0$, and thus (19) reduces to

$$u_{D_2} + \Delta\psi_0 = \mathcal{R}\, i_D(u_{D_2}), \tag{20}$$

where $\Delta\psi_0 := \psi_0|_{\Gamma_{D_2}} - \psi_0|_{\Gamma_{D_1}}$ is the built-in potential and $u_{LPS} := u_{D_2}$ the *LPS voltage* or the *LPS signal*, our quantity of interest.

Notice that (20) is an implicit equation for u_{D_2} since i_D depends implicitly on u_{D_2}, via the van Roosbroeck system (1). Once we have found a solution $(\psi, \varphi_n, \varphi_p)$ to the van Roosbroeck system where u_{D_2} enters the Dirichlet boundary condition (6), we compute the current i_D via (7). In [3] and the references therein, related coupled models are analyzed in detail. In particular, the existence of a solution is proven in case of a vanishing generation rate G and more complicated circuits [3, Theorem 1]. We state the result here, adapted as far as possible to our specific setting:

Theorem 1 (Existence and boundedness of solution)**.** *The van Roosbroeck model* (1) *for* $G \equiv 0$ *coupled with* (19) *and supplied with boundary conditions* (5), (6) *admits a solution* $(\psi, \varphi_n, \varphi_p) \in (H^1(\Omega) \cap L_\infty(\Omega))^3$*. Moreover, any solution satisfies the estimates* $\inf_{\Gamma_D} \psi_0 + \min_i u_{D_i} \leq \psi \leq \sup_{\Gamma_D} \psi_0 + \max_i u_{D_i}$,$\min_i u_{D_i} \leq \varphi_n, \varphi_p \leq \max_i u_{D_i}$.

3 Tauc theory

In this section, we summarize and work out the theoretical framework first developed by Tauc [22]. We will use his theoretical results to validate our simulation results. Starting with his observations we derive three theoretical results.

As a starting point Tauc assumed a 1D circular geometry as shown in Figure 6, assuming that the segment from $\mathbf{b}$ to $\mathbf{c}$ is illuminated with monochromatic light. The sample contacts are denoted by $\mathbf{a}'$ and $\mathbf{a}$. The photoinduced LPS voltage difference is measured between both contacts, namely $u_{LPS} = \psi(\mathbf{a}') - \psi(\mathbf{a})$. It is assumed also that the contact positions are far enough from the illuminated region to prevent that excess carrier densities reach them. Furthermore we suppose that the sample thickness is sufficiently small compared to the reciprocal of the absorption coefficient in the direction of the radiating field (hence we can work indeed on a circle instead of an annulus). Additionally, the transverse direction is assumed much thinner than the beam diameter, so that the generation rate can be assumed constant in the entire segment from $\mathbf{b}$ to $\mathbf{c}$.

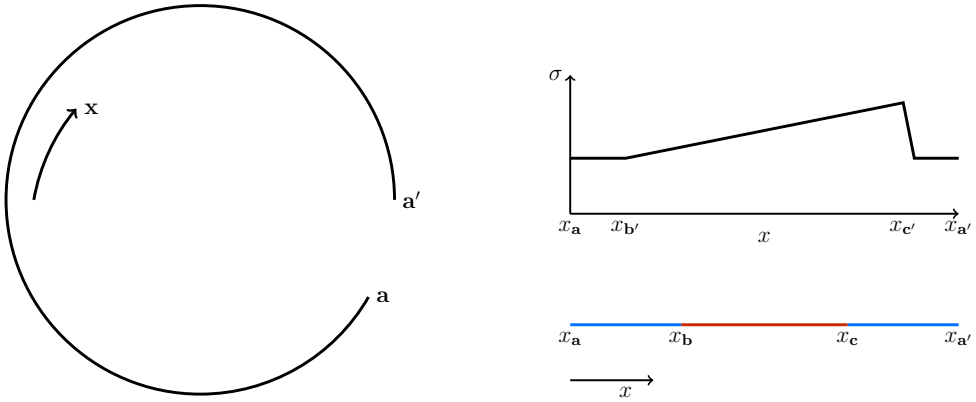

Figure 6: 1D sample geometry. The red region represents the illuminated portion of the sample; the two contacts are placed at the sample boundaries and are marked by $\mathbf{a}$ and $\mathbf{a}'$. As an inlay the conductivity profile $\sigma(x)$ assumed for case (III) is shown.

We define the line integral of the electric vector field $\mathbf{E}$ to be

$$\int_\gamma \mathbf{E}(\mathbf{x}) \cdot d\mathbf{x} := \int_{x_{\mathbf{a}}}^{x_{\mathbf{a}'}} \mathbf{E}(\boldsymbol{\gamma}(x)) \cdot \boldsymbol{\gamma}'(x) dx, \tag{21}$$

where $\boldsymbol{\gamma}\colon \mathbb{R} \to \mathbb{R}^2$ is defined by

$$\boldsymbol{\gamma}(x) = \begin{pmatrix} \cos(x) \\ \sin(x) \end{pmatrix}$$

such that $\boldsymbol{\gamma}(x_{\mathbf{a}}) = \mathbf{a}$ and $\boldsymbol{\gamma}(x_{\mathbf{a}'}) = \mathbf{a}'$. For the electric field Tauc assumed

$$\mathbf{E}(\boldsymbol{\gamma}(x)) = F(x)\boldsymbol{\gamma}'(x),$$

with

$$F(x) = U_T \frac{\mu_p \frac{d}{dx} p(x) - \mu_n \frac{d}{dx} n(x)}{\mu_p p(x) + \mu_n n(x)}.$$

This expression for the electric field in 1D is derived from (8) for $F = \frac{d}{dx}\psi$. That is, (21) becomes

$$u_{LPS} = \psi(\mathbf{a}') - \psi(\mathbf{a}) = -\int_\gamma \mathbf{E}(\mathbf{x}) \cdot d\mathbf{x} = -\int_{x_{\mathbf{a}}}^{x_{\mathbf{a}'}} F(x) dx = -U_T \int_{x_{\mathbf{a}}}^{x_{\mathbf{a}'}} \frac{\mu_p \frac{d}{dx} p - \mu_n \frac{d}{dx} n}{\mu_p p + \mu_n n} dx. \tag{22}$$

This formula will be the basis of many of the following observations.

We will introduce notation to make clear how some quantity within a sample illuminated at laser spot position $\mathbf{x}_0$ is perturbed from equilibrium values (denoted with the subscript *eq*) by a certain excess amount. Namely,

$$\begin{aligned} n(\mathbf{x}) &= n_{eq}(\mathbf{x}) + \Delta n(\mathbf{x}-\mathbf{x}_0), \quad p(\mathbf{x}) = p_{eq}(\mathbf{x}) + \Delta p(\mathbf{x}-\mathbf{x}_0), \\ \rho(\mathbf{x}) &= \rho_{eq}(\mathbf{x}) + \Delta \rho(\mathbf{x}-\mathbf{x}_0), \quad \sigma(\mathbf{x}) = \sigma_{eq}(\mathbf{x}) + \Delta \sigma(\mathbf{x}-\mathbf{x}_0). \end{aligned} \tag{23}$$

Here σ and ρ refer respectiveley to the conductivity and the resistivity defined as

$$\sigma := q(\mu_n n + \mu_p p), \qquad \rho := 1/\sigma. \tag{24}$$

If there is no illumination $G = 0$ then also no excess quantities will be generated and all four quantities are given by their respective equilibrium values. In the following several assumptions will be needed which we will collect here first:

(A1) The equilibrium electron density dominates the equilibrium hole density: $n_{eq} \gg p_{eq}$.

(A2) The equilibrium electron density is approximately given by the donor doping value: $n_{eq} \approx N_D$.

(A3) The doping variations are comparatively small to the doping offset: $N_D(\mathbf{x}) = N_{D0} + \Delta N_D(\mathbf{x})$ with $N_{D0} \gg \max_{\mathbf{x}\in\Omega} |\Delta N_D(\mathbf{x})|$.

(A4) The laser generates as many electrons as holes: $\Delta n = \Delta p$.

(A5) We have weak illumination, that is $\Delta\sigma \ll \sigma_{eq}$. This case is by physicists referred to as *low injection conditions*. In this case, we have also

$$\frac{\sigma_{eq}}{\Delta\sigma + \sigma_{eq}} \approx 1 - \frac{\Delta\sigma}{\sigma_{eq}}.$$

(A6) The illuminated area is relatively small with respect to the doping variation.

Assumption (A1) and (A2) imply

$$\sigma_{eq} = q(\mu_n n_{eq} + \mu_p p_{eq}) \approx q\mu_n n_{eq} \approx q\mu_n N_D. \tag{25}$$

Tauc analyzed theoretically the three following cases [22]:

1 **non-illuminated semiconductor:** If our sample is not illuminated, the charge carrier densities are given by their respective equilibrium values, namely

$$n(x) = n_{eq}(x), \qquad p(x) = p_{eq}(x) = \frac{n_i(x)^2}{n(x)}.$$

If $x_{\mathbf{a}} = x_{\mathbf{a}'}$, we know by the fundamental theorem of calculus for line integrals that (22) vanishes. However, since we need to measure the LPS voltage difference we cannot close the circuit entirely. However, it is safe to assume that $n_{eq}(x_{\mathbf{a}}) = n_{eq}(x_{\mathbf{a}'})$. In this case (22) will vanish as well since

$$u_{LPS} = -\int_{x_{\mathbf{a}}}^{x_{\mathbf{a}'}} F(x)dx = -U_T \int_{x_{\mathbf{a}}}^{x_{\mathbf{a}'}} \frac{n_{eq}'}{n_{eq}} dx = -U_T \Big[\log(n_{eq})\Big]_{x_{\mathbf{a}}}^{x_{\mathbf{a}'}} = 0. \tag{26}$$

2 **illuminated homogeneous semiconductor:** We use the notation introduced in (23). Since the semiconductor is homogeneous we have $N_D = 0$ which implies that n_{eq} and p_{eq} are constants. Since $x_{\mathbf{a}}$ and $x_{\mathbf{a}'}$ are far away from the illuminated area, we have $\Delta n(x_{\mathbf{a}}) = \Delta n(x_{\mathbf{a}'}) = 0$. In this case (22) vanishes as well since we have by case 1 and (A4) that

$$\begin{aligned} u_{LPS} &= -U_T \int_{x_{\mathbf{a}}}^{x_{\mathbf{a}'}} \frac{\mu_p \frac{d}{dx} p - \mu_n \frac{d}{dx} n}{\mu_p p + \mu_n n} dx \\ &= -U_T \int_{x_{\mathbf{a}}}^{x_{\mathbf{a}'}} \frac{(\mu_p - \mu_n)\frac{d}{dx}\Delta n}{\mu_p(p_{eq} + \Delta n) + \mu_n(n_{eq} + \Delta n)} dx \\ &= -U_T \frac{\mu_p - \mu_n}{\mu_p + \mu_n} \int_{x_{\mathbf{a}}}^{x_{\mathbf{a}'}} \frac{(\mu_p + \mu_n)\frac{d}{dx}\Delta n}{\mu_p p_{eq} + \mu_n n_{eq} + (\mu_p + \mu_n)\Delta n} dx \\ &= -U_T \frac{\mu_p - \mu_n}{\mu_p + \mu_n} \log\left(\mu_p p_{eq} + \mu_n n_{eq} + (\mu_p + \mu_n)\Delta n\right)\Big|_{x_{\mathbf{a}}}^{x_{\mathbf{a}'}} \\ &= 0. \end{aligned}$$

3 **illuminated inhomogeneous semiconductor:** Only this final case leads to a nonvanishing LPS voltage. Since the analysis is more complicated, Tauc makes some additional assumptions on the conductivity, shown in Figure 6. A constant gradient is assumed in $[x_{\mathbf{b}'}, x_{\mathbf{c}'}]$. Both values, $x_{\mathbf{b}'}$ and $x_{\mathbf{c}'}$, are chosen such that no excess charge carrier Δn generated in $[x_{\mathbf{b}}, x_{\mathbf{c}}]$ may reach $x_{\mathbf{b}'}$ or $x_{\mathbf{c}'}$ by diffusion. Under this assumption Tauc can show that

$$u_{LPS} = -U_T \frac{2}{\bar{\mu}} \log\left[\frac{1 + \frac{\Delta\sigma}{\sigma(x_{\mathbf{c}})}}{1 + \frac{\Delta\sigma}{\sigma(x_{\mathbf{b}})}}\right] = -U_T \frac{2}{\bar{\mu}} \left(\log\left[\frac{\sigma(x_{\mathbf{c}})}{\sigma(x_{\mathbf{b}})}\right] - \log\left[\frac{\sigma(x_{\mathbf{c}}) + \Delta\sigma}{\sigma(x_{\mathbf{b}}) + \Delta\sigma}\right]\right), \tag{27}$$

where again $\Delta\sigma$ is the conductivity variation due to illumination and $\bar{\mu} = 1 + \frac{\mu_n}{\mu_p}$.

Using Tauc' result we make the following predictions on the LPS signal.

Theorem 2. *From Tauc' model it follows that the LPS voltage*

(I) features a logarithmic growth for low laser powers

$$\begin{aligned} \lim_{P\to 0} u_{LPS}(P) = &- U_T \frac{2}{\bar{\mu}} \times \\ &\left(\log\left[\frac{N_D(x_{\mathbf{c}})}{N_D(x_{\mathbf{b}})}\right] - \log\left[\frac{N_D(x_{\mathbf{c}})}{N_D(x_{\mathbf{b}})} + \kappa P \frac{\bar{\mu}(N_D(x_{\mathbf{b}}) - N_D(x_{\mathbf{c}}))}{N_D(x_{\mathbf{b}})} + O(P^2)\right]\right), \end{aligned} \tag{28}$$

(II) for low and high laser powers saturates

$$\lim_{P\to\infty} u_{LPS}(P) = -U_T \frac{2}{\bar{\mu}} \log\left[\frac{N_D(x_{\mathbf{c}})}{N_D(x_{\mathbf{b}})}\right]. \tag{29}$$

(III) is proportional to the doping gradient

$$u_{LPS}(x_0) \approx -\frac{U_T}{q\mu_n N_{D0}} \frac{2}{\bar{\mu}} N_D'(x_0) \int_{x_0-\delta/2}^{x_0+\delta/2} \frac{1}{N_{D0}} \Delta\sigma(x - x_0) dx \tag{30}$$

for some small $\delta > 0$.

Proof. Inserting the conductivity defined in (24), the photoinduced conductivity variation $\Delta\sigma = q\Delta n(\mu_n + \mu_p)$ and the equilibrium conductivity variation $\sigma(x_\mathbf{b}) = q\mu_n N_D(x_\mathbf{b})$ in (27), we obtain

$$u_{LPS} = -U_T \frac{2}{\bar{\mu}} \left(\log\left[\frac{N_D(x_\mathbf{c})}{N_D(x_\mathbf{b})}\right] - \log\left[\frac{N_D(x_\mathbf{c}) + \Delta n\bar{\mu}}{N_D(x_\mathbf{b}) + \Delta n\bar{\mu}}\right]\right). \tag{31}$$

This equation holds true for any mono-doped semiconductor. If the SRH recombination is dominant (as it is plausible for silicon), the excess carrier density will be proportional to the laser pump power $\Delta n = \kappa P$ for some $\kappa > 0$. Hence,

$$u_{LPS} = -U_T \frac{2}{\bar{\mu}} \left(\log\left[\frac{N_D(x_\mathbf{c})}{N_D(x_\mathbf{b})}\right] - \log\left[\frac{N_D(x_\mathbf{c}) + \kappa P\bar{\mu}}{N_D(x_\mathbf{b}) + \kappa P\bar{\mu}}\right]\right). \tag{32}$$

For low and high laser powers this leads respectiveley to (28) and (29).

To show that the LPS voltage under certain conditions is proportional to the gradient of the doping concentration, we start again from (22). By the first result for non-illuminated semiconductors we obtain

$$\begin{aligned} u_{LPS} &= -\int_{x_\mathbf{a}}^{x_\mathbf{b}} F(x; G=0)dx - \int_{x_\mathbf{b}}^{x_\mathbf{c}} F(x; G\neq 0)dx - \int_{x_\mathbf{c}}^{x_{\mathbf{a}'}} F(x; G=0)dx \\ &= -\int_{x_\mathbf{a}}^{x_{\mathbf{a}'}} F(x; G=0)dx + \int_{x_\mathbf{b}}^{x_\mathbf{c}} F(x; G=0)dx - \int_{x_\mathbf{b}}^{x_\mathbf{c}} F(x; G\neq 0)dx \\ &= \int_{x_\mathbf{b}}^{x_\mathbf{c}} F(x; G=0)dx - \int_{x_\mathbf{b}}^{x_\mathbf{c}} F(x; G\neq 0)dx. \end{aligned}$$

By arguments similar to the case for non-illuminated semiconductors, see (26), we obtain for the first integral

$$\int_{x_\mathbf{b}}^{x_\mathbf{c}} F(x; G=0)dx = -U_T\Big[\log(n_{eq})\Big]_{x_\mathbf{b}}^{x_\mathbf{c}} =: C_{nl} = \text{const.}$$

We focus on the second integral. By the definition of the conductivity and (A4), we find

$$\begin{aligned} \int_{x_\mathbf{b}}^{x_\mathbf{c}} F(x; G\neq 0) &= U_T \int_{x_\mathbf{b}}^{x_\mathbf{c}} \frac{\mu_p \frac{d}{dx}p - \mu_n \frac{d}{dx}n}{\mu_p p + \mu_n n}dx \\ &= U_T \int_{x_\mathbf{b}}^{x_\mathbf{c}} \frac{\mu_p \frac{d}{dx}(p_{eq}+\Delta n) - \mu_n \frac{d}{dx}(n_{eq}+\Delta n)}{\sigma_{eq}+\Delta\sigma}dx \\ &= U_T \int_{x_\mathbf{b}}^{x_\mathbf{c}} \frac{(\mu_p - \mu_n)\frac{d}{dx}\Delta n - \mu_p \frac{p_{eq}}{n_{eq}}\frac{d}{dx}n_{eq} - \mu_n \frac{d}{dx}n_{eq}}{\sigma_{eq}+\Delta\sigma}dx \end{aligned}$$

Since (4) implies that $\frac{d}{dx}p_{eq} = -\frac{p_{eq}}{n_{eq}}\frac{d}{dx}n_{eq}$, the final equality holds. Considering that

$$\Delta\sigma(x - x_0) = (\mu_p + \mu_n)\Delta n(x - x_0) \qquad \text{and} \qquad \sigma_{eq} = q(\mu_n n_{eq} + \mu_p p_{eq}),$$

we obtain

$$\int_{x_\mathbf{b}}^{x_\mathbf{c}} F(x; G\neq 0) = U_T \frac{\mu_p - \mu_n}{\mu_p + \mu_n} \int_{x_\mathbf{b}}^{x_\mathbf{c}} \frac{\frac{d}{dx}\Delta\sigma}{\sigma_{eq}+\Delta\sigma}dx - U_T \int_{x_\mathbf{b}}^{x_\mathbf{c}} \frac{\sigma_{eq}}{\sigma_{eq}+\Delta\sigma}\frac{\frac{d}{dx}n_{eq}}{n_{eq}}dx.$$

Using (A5) and the partial integration

$$\int_{x_\mathbf{b}}^{x_\mathbf{c}} \frac{\frac{d}{dx}\Delta\sigma}{\sigma_{eq}}dx = \int_{x_\mathbf{b}}^{x_\mathbf{c}} \rho_{eq}\frac{d}{dx}\Delta\sigma dx = \rho_{eq}\Delta\sigma\Big|_{x_\mathbf{b}}^{x_\mathbf{c}} - \int_{x_\mathbf{b}}^{x_\mathbf{c}} \Delta\sigma\frac{d}{dx}\rho_{eq}dx = -\int_{x_\mathbf{b}}^{x_\mathbf{c}} \Delta\sigma\frac{d}{dx}\rho_{eq}dx$$

we find

$$\int_{x_{\mathbf{b}}}^{x_{\mathbf{c}}} F(x; G \neq 0) = -U_T \frac{\mu_p - \mu_n}{\mu_p + \mu_n} \int_{x_{\mathbf{b}}}^{x_{\mathbf{c}}} \Delta\sigma \frac{d}{dx}\rho_{eq} dx + C_{nl} + U_T \int_{x_{\mathbf{b}}}^{x_{\mathbf{c}}} \frac{\Delta\sigma}{\sigma_{eq}} \frac{\frac{d}{dx} n_{eq}}{n_{eq}} dx.$$

Combining the above result with the fact that (25) yields

$$\frac{\frac{d}{dx} n_{eq}}{n_{eq}} = -\sigma_{eq} \frac{d}{dx}\rho_{eq}, \tag{33}$$

we obtain

$$u_{LPS} = U_T \left(\frac{2}{\bar{\mu}}\right) \int_{x_{\mathbf{b}}}^{x_{\mathbf{c}}} \Delta\sigma(x - x_0) \frac{d}{dx}\rho_{eq}(x) dx$$

Let us assume that $x_{\mathbf{b}} = x_0 - \delta/2$ and $x_{\mathbf{c}} = x_0 + \delta/2$ for some $\delta > 0$ which is by assumption (A6) relatively small, then

$$u_{LPS} \approx U_T \left(\frac{2}{\bar{\mu}}\right) \left(\frac{d}{dx}\rho_{eq}(x)\right) \Big|_{x=x_0} \int_{x_0-\delta/2}^{x_0+\delta/2} \Delta\sigma(x - x_0) dx.$$

By (33), (25) and (A3), we deduce (30). □

4 Finite volume discretization

In this section, we present a Voronoï finite volume technique [13, 12, 11, 21]. Similar as for finite elements, we start by partitioning the domain Ω into non-intersecting, convex polyhedral control volumes ω_k such that $\Omega = \bigcup_{k=1}^{N_{\text{vert}}} \omega_k$. Unlike for finite elements, these control volumes need not to be triangular but fulfill the following orthogonality condition: we associate with each control volume ω_k a node $\mathbf{x}_k \in \omega_k$. For every boundary intersecting control volume, we demand that this node lies on the boundary $\mathbf{x}_k \in \partial\Omega \cap \omega_k$. Assuming that the partition is admissible in the sense of [9], that is for two adjacent control volumes ω_k and ω_l, the edge $\overline{\mathbf{x}_k\mathbf{x}_l}$ of length h_{kl} is orthogonal to $\partial\omega_k \cap \partial\omega_l$, the normal vectors to $\partial\omega_k$ can be calculated by $\boldsymbol{\nu}_{kl} = (\mathbf{x}_l - \mathbf{x}_k)/\|\mathbf{x}_l - \mathbf{x}_k\|$. For each control volume ω_k,

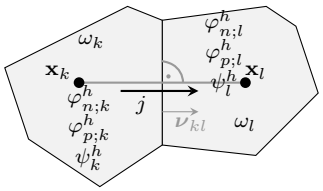

Figure 7: Two adjacent control volumes ω_k and ω_l with corresponding notation.

the finite volume discretization is given by the three equations:

$$\sum_{\omega_l \in \mathcal{N}(\omega_k)} |\partial\omega_k \cap \partial\omega_l| j_{\psi;k,l} = q|\omega_k| \left(C_k + p_k^h - n_k^h\right), \tag{34a}$$

$$\sum_{\omega_l \in \mathcal{N}(\omega_k)} |\partial\omega_k \cap \partial\omega_l| j_{n;k,l} = +q|\omega_k| R_k, \tag{34b}$$

$$\sum_{\omega_l \in \mathcal{N}(\omega_k)} |\partial\omega_k \cap \partial\omega_l| j_{p;k,l} = -q|\omega_k| R_k. \tag{34c}$$

We denote with $\mathcal{N}(\omega_k)$ the set of all control volumes neighboring ω_k. In 2D, the measure $|\partial\omega_k \cap \partial\omega_l|$ corresponds to the length of the boundary line segment and in 3D to the area of the intersection of the boundary surfaces. Furthermore, in 2D the measure $|\omega_k|$ is given by the area and in 3D by the volume of the control volume ω_k. The unknowns ψ_k^h, $\varphi_{n;k}^h$, $\varphi_{p;k}^h$ correspond to the electrostatic potential as well as the quasi-Fermi potentials for electrons and holes evaluated at node $\mathbf{x}_k$. Accordingly, n_k^h, p_k^h, R_k and C_k are defined as

$$n_k^h = N_c \mathcal{F}\big(\eta_n(\psi_k^h, \varphi_{n;k}^h)\big), \qquad C_k = C(\mathbf{x}_k), \tag{35a}$$

$$p_k^h = N_v \mathcal{F}\big(\eta_p(\psi_k^h, \varphi_{p;k}^h)\big), \qquad R_k = R\big(n_k^h, p_k^h\big). \tag{35b}$$

The notation is explained visually in Figure 7.

Note that the doping profile C and the recombination rate R are given. The numerical fluxes $j_{\psi;k,l}$, $j_{n;k,l}$ and $j_{p;k,l}$ approximate respectively $-\varepsilon_0\varepsilon_r \nabla\psi \cdot \boldsymbol{\nu}_{kl}$, $\mathbf{j}_n \cdot \boldsymbol{\nu}_{kl}$ and $\mathbf{j}_p \cdot \boldsymbol{\nu}_{kl}$ on the interfaces between two adjacent control volumes ω_k and ω_l. These fluxes can be expressed as functions depending nonlinearly on the values ψ_k^h, $\varphi_{n;k}^h$, $\varphi_{p;k}^h$ and ψ_l^h, $\varphi_{n;l}^h$, $\varphi_{p;l}^h$. The flux corresponding to the electrostatic displacement is approximated by

$$j_{\psi;k,l} = -\varepsilon_0\varepsilon_r \frac{\psi_l^h - \psi_k^h}{\|\mathbf{x}_l - \mathbf{x}_k\|}.$$

Next, we discuss numerical flux approximations which appear in the discretizations of the continuity equations. Choosing the numerical fluxes $j_{n;k,l}$ and $j_{p;k,l}$ correctly is a rather delicate issue as the wrong choice may lead to either instabilities or the violation of thermodynamic principles. Scharfetter and Gummel presented in [20] a suitable choice for Boltzmann statistics. The constant Scharfetter-Gummel flux is given by

$$j_{n;k,l} = -\frac{q\mu_n N_c U_T}{x_l - x_k}\left(\exp\left(\eta_{n;k}^h\right) B\left(-\frac{\psi_l^h - \psi_k^h}{U_T}\right) - \exp\left(\eta_{n;l}^h\right) B\left(\frac{\psi_l^h - \psi_k^h}{U_T}\right)\right) \tag{36}$$

with $\eta_{n;k}^h = \eta_n(\psi_k^h, \varphi_{n;k}^h)$ and $\eta_{n;l}^h = \eta_n(\psi_l^h, \varphi_{n;l}^h)$. The Bernoulli function is given by $B(\eta) = \eta/(e^\eta - 1)$. A similar expression can be derived for the hole flux. We point out that only in the Boltzmann regime this flux is thermodynamically consistent in the sense that constant quasi-Fermi potentials imply that the flux vanishes.

4.1 Solution strategy for nonlinear boundary condition

In this section, we detail how we solve the van Roosbroeck model, considering the implicit relationship (20) for the contact voltage u_{D_2}. We need to find the root of the function

$$\begin{aligned} F(u_{D_2}) &:= u_{D_2} + \Delta\psi_0 - R\, i_D(u_{D_2}) \\ &= u_{D_2} + \Delta\psi_0 - R \int_{\Gamma_{D_2}} \boldsymbol{\nu} \cdot (\boldsymbol{J}_n(\mathbf{x}; u_{D_2}) + \boldsymbol{J}_p(\mathbf{x}; u_{D_2}))d\sigma(\mathbf{x}). \end{aligned}$$

Remember that in order to compute the second term, we need to solve the van Roosbroeck system (1). So evaluating F corresponds to solving the van Roosbroeck system once. Since we do not know the derivative of F with respect to u_{D_2}, we apply for $\ell = 2, 3, \ldots$ the secant method

$$u_{D_2}^{\ell+1} = u_{D_2}^{\ell} - F(u_{D_2}^{\ell}) \frac{u_{D_2}^{\ell} - u_{D_2}^{\ell-1}}{F(u_{D_2}^{\ell}) - F(u_{D_2}^{\ell-1})}, \tag{37}$$

using two starting values $u_{D_2}^0$ and $u_{D_2}^1$.

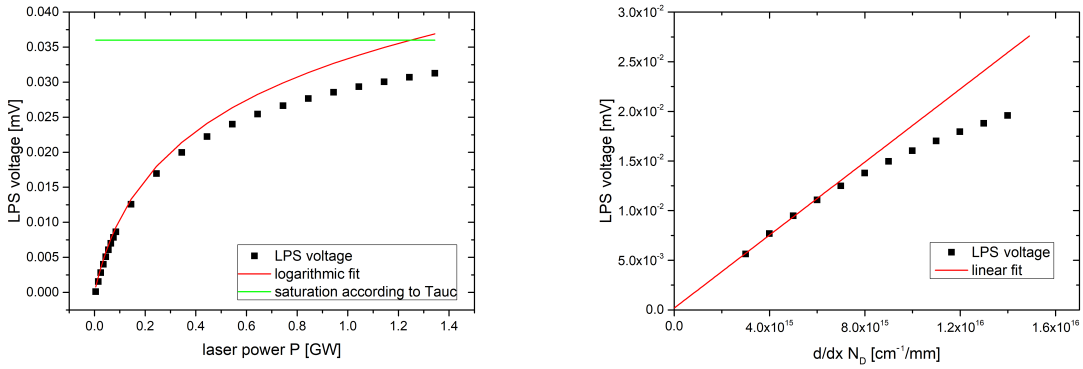

Figure 8: Tauc model: LPS voltage as a function of the laser power at $x_0 = 0\,\text{mm}$ for $N_{D0} = 1 \times 10^{16}\,\text{cm}^{-1}$ (left) and LPS voltage as a function of the doping gradient $\frac{d}{dx}N_D = N_{D0}/15\,\text{mm}$ at $x_0 = 0\,\text{mm}$ (right).

5 Numerical simulation results

In this section, we present different simulations results. Our simulations are based on the open-source tool `ddfermi` [8].

5.1 Tauc model

We compare our simulation results to the three statements in Theorem 2. Due to the discussion in Section 3 the Tauc model can be viewed as one-dimensional LPS model, see Section 2.6.1, with a special conductivity profile σ. For the sake of simplicity, we set $x_{\mathbf{a}} = x_{\mathbf{b}'} = -1.5\,\text{mm}$ as well as $x_{\mathbf{a}'} = x_{\mathbf{c}'} = 1.5\,\text{mm}$ and assume the sample is illuminated at the center. The beam width $\sigma_L = 10\,\mu\text{m}$ is chosen significantly smaller than the illuminated area $x_{\mathbf{c}} - x_{\mathbf{b}} = 2.5\,\text{mm}$ to avoid excess carrier diffusion. We define $\sigma \approx \sigma_{eq}$ under low injection conditions (see (A5)) indirectly via (25) and

$$N_D(x) = \begin{cases} N_{D0}(1 + \frac{x}{15\,\text{mm}}), & x \leq 1\,\text{mm}, \\ N_{D0}(1.4 - \frac{x}{3\,\text{mm}}), & \text{else}. \end{cases} \tag{38}$$

As predicted by (I) in Theorem 2, our simulations, shown in Figure 8 left panel, feature a logarithmic behavior for small laser powers. It must be pointed out that the simulation results were shifted by a non-physical offset which leads to $U(P = 0) \neq 0$. By calculating this offset and shifting the data accordingly we could guarantee that $U(P = 0) = 0$ is fulfilled. The saturation described by (II) in Theorem 2 can also be observed in our simulation. The green line defines the maximum voltage according to (II), which is in perfect agreement with our simulation results. In [15] the authors give a physical argument why this is likely related to the screening effect. Finally, we analyze statement (III) in Theorem 2 for small variations of the doping profile $N_D(x)$. The simulation result in Figure 8 (right panel) shows a linear dependency of the doping variation $\frac{d}{dx}N_D = N_{D0}/15\,\text{mm}$ for small LPS voltages. For larger values of the doping variation LPS voltage and doping variation deviate from each other nonlinearly. In this case, the low injection assumption (A5) is violated so that no linear relationship is guaranteed anymore by Theorem 2. In summary, we note that our simulation results agree with the theory.

5.2 2D LPS model

Next, we simulate a 2D LPS model from Section 2.6.2. We define the doping profile

$$N_D = N_{D0}\left(1 + 0.2\sin\left(2\pi\frac{x}{100\,\mu\text{m}}\right)\right), \tag{39}$$

with $N_{D0} = 1 \times 10^{16}\,\text{cm}^{-2}$.

The numerical challenge we face here is that on the one hand due to the large diffusion length in silicon (up to the order of millimeters) the sample needs to be several millimeters long. On the other hand, the penetration depth of the laser $d_A = 4.8\,\mu\text{m}$ is three orders of magnitude smaller than any suitable sample length. The remaining parameters can be found in Appendix A.1.

A mesh with constant mesh size would either be inefficient with respect to the simulation time and or lead to a poor resolution of the laser beam profile. To avoid this, we designed an anisotropic mesh which resolves only the laser spot position well. This mesh is shown in Figure 9 for different zoom levels. The colors correspond to the simulated quasi Fermi potential for holes φ_p. Since $N_A = 0\,\text{cm}^{-3}$, the shape of φ_p is mainly given by the generation rate G and the sample inherent diffusion length. It can be seen that φ_p is decreasing fast in x direction, hence the directly linked excess charge carrier distribution Δp is also decreasing fast by (2). As discussed above this is required for our simulation. The secant method (37) converges usually within 3-4 steps to a tolerance of 1×10^{-9}.

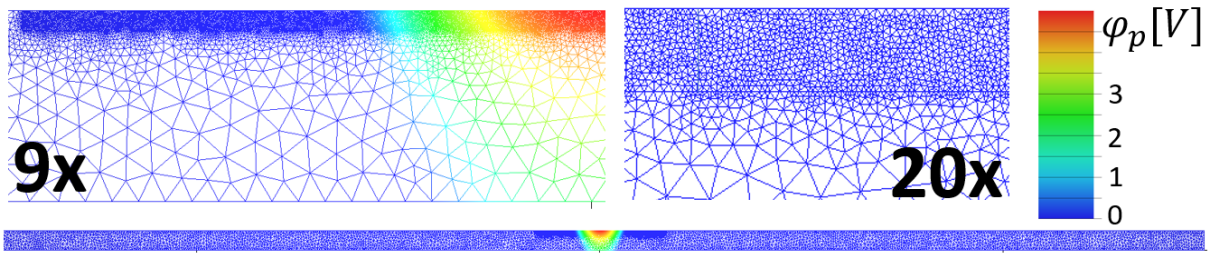

Figure 9: Full length 2D mesh geometry (bottom row) with different zoom levels (top row). The colors correspond to the quasi Fermi potential values for holes φ_p for the laser power $P = 200\,\text{W}$ and laser spot position $x_0 = 0$.

Next we vary the laser spot position x_0 and compute the LPS voltage u_{LPS} for each position, shown in Figure 10 (right panel). On the right axis the doping variation (red) is shown, revealing a wavelength $\lambda = 100\,\mu\text{m}$. The LPS voltage (marked in black and shown on the left axis) features a variation in agreement with the doping variation wave length. We stress again the fact, that this result agrees with (III) in Theorem 2 even though we simulate a more complex geometry. Having a closer look at the maxima and minima of the doping gradient, it can be observed that they do not perfectly match the simulated voltages. This can be explained by the fact that in (30) the LPS voltage is only approximately proportional to the doping variation. Also the first peak is not perfectly resolved since the mesh is significantly coarser in this area due to our anisotropic mesh.

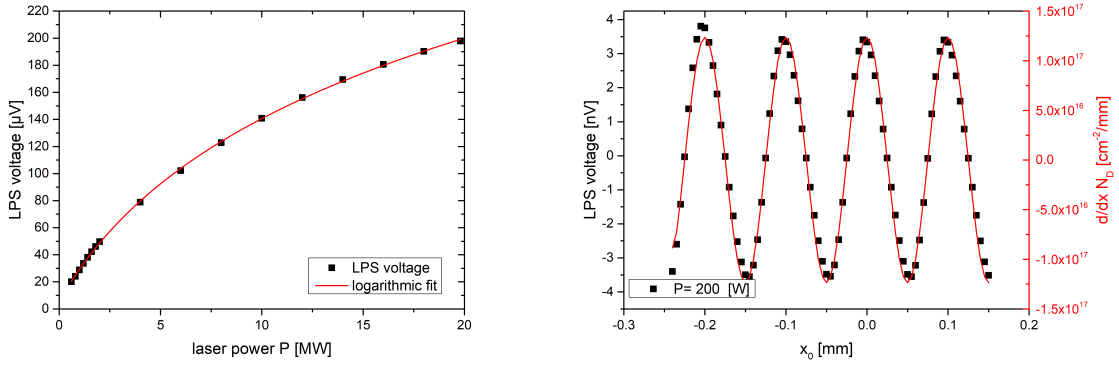

Figure 10: 2D simulation results: LPS voltage as a function of the laser power at $x_0 = 0\,\text{mm}$ with $N_{D0} = 1 \times 10^{16}\,\text{cm}^{-2}$ (left) and the LPS voltage for varying laser spot position (right). The LPS voltage is shown on the left axis in black and the doping variation profile on the right axis in red ($N_{D0} = 1 \times 10^{16}\,\text{cm}^{-2}$). The first peak is not perfectly resolved since the mesh is significantly coarser in this area due to our anisotropic mesh.

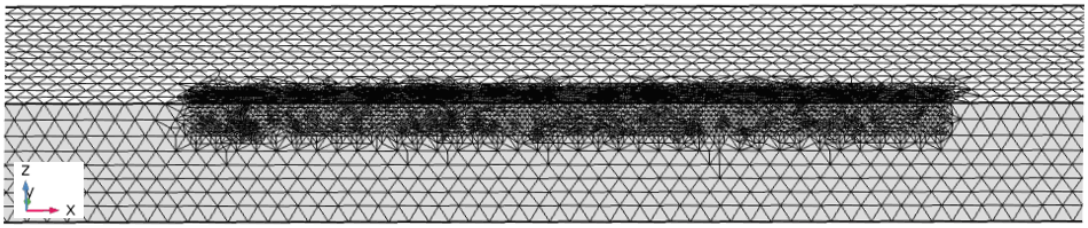

Figure 11: Anisotropic 3D mesh

5.3 3D LPS model

Finally, we simulate a full 3D tabletop setup described in Section 2.6.3 using again an anisotropic mesh, shown in Figure 11 with approximately two million nodes. The doping profile is defined by

$$N_D(x,y,z) = N_{D0}\left(1 + 0.2\sin\left(2\pi\frac{x}{100\,\mu\text{m}}\right)\right). \tag{40}$$

The remaining parameters are summarized in Appendix A.1. We plot the simulated quasi Fermi potentials, the densities, the electrostatic potential as well as the generation rate in Figure 12. The secant method (37) converges usually within 3-4 steps to a tolerance of 1×10^{-9}.

As for the 2D case, we observe again (cf. Theorem 2) a logarithmic behavior of the LPS voltage with respect to the laser power (I), an eventual saturation (II) as well as a sinusoidal variation of the signal (III), matching the gradient of doping profile (40) in x direction, see Figure 13 left and right panel. Only near the extrema one can notice a small deviation which we also observed in the 2D case.

In 3D, we also compare LPS voltages $u_{LPS}(P)$ for different base doping levels N_{D0} in Figure 14, left panel. Generally, for low laser powers P the resulting LPS voltage is nearly independent of the base doping level. For higher laser powers the signal saturates due to the screening effect. In this regime, the valleys in the doping are completely filled with free charge carriers so that the doping variations are not measurable anymore. That is, once the screening effect dominates, no meaningful measurements can be obtained. Naturally, our simulations confirm that this happens faster for smaller base doping levels and predict for a given base doping level which laser powers still give meaningful results. For example,

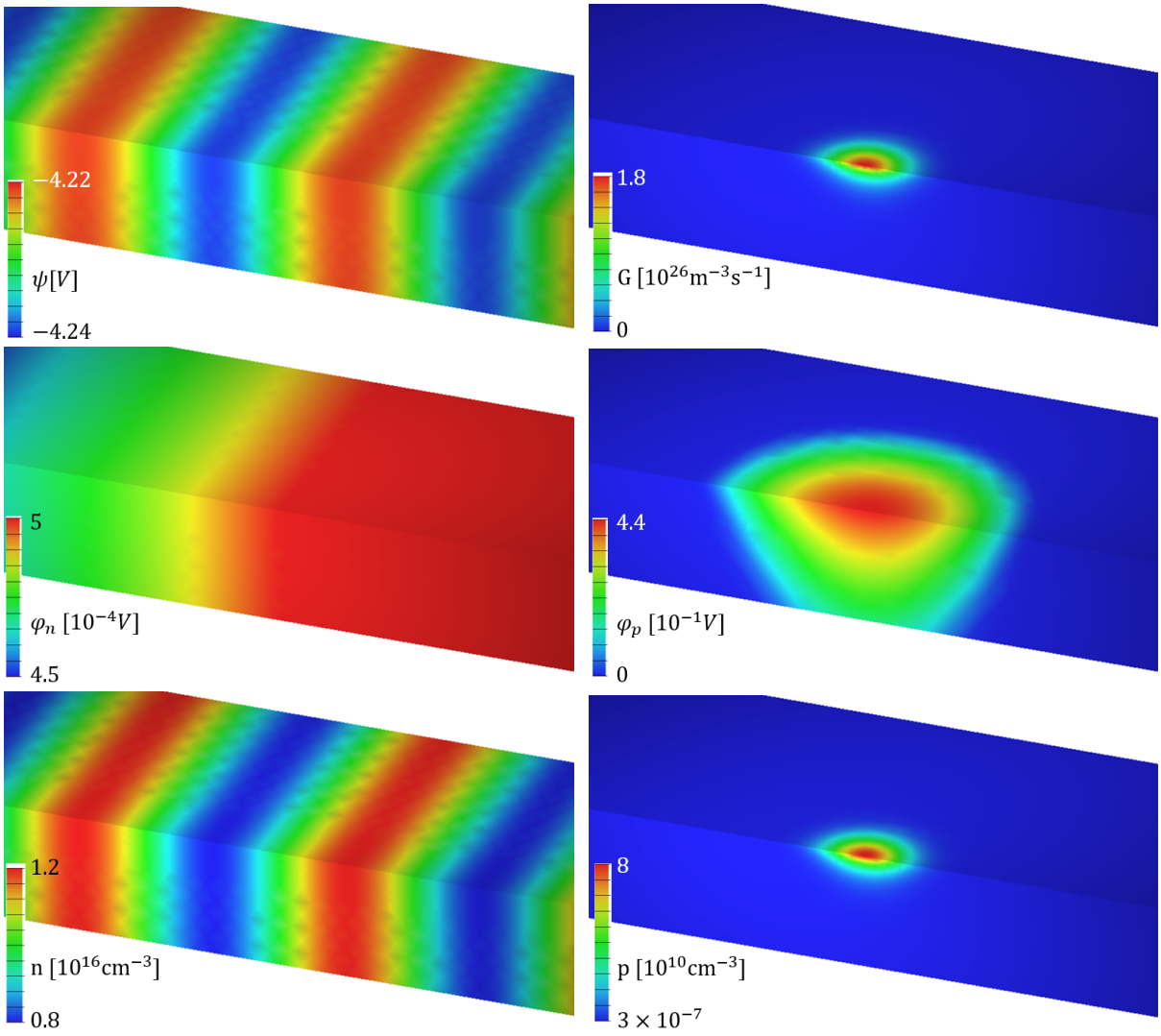

Figure 12: 3D simulation result for $P = 2\,\text{mW}$, $(x_0, y_0)^T = (0\,\text{mm}, 0\,\text{mm})^T$ and $N_{D0} = 1 \times 10^{16}\,\text{cm}^{-3}$. We show the electrostatic potential ψ (upper left panel), the resulting generation rate G (upper right panel), the quasi Fermi potentials φ_n,φ_p for electrons and holes (middle panels). The related charge carrier densities n, p are shown in the bottom panels.

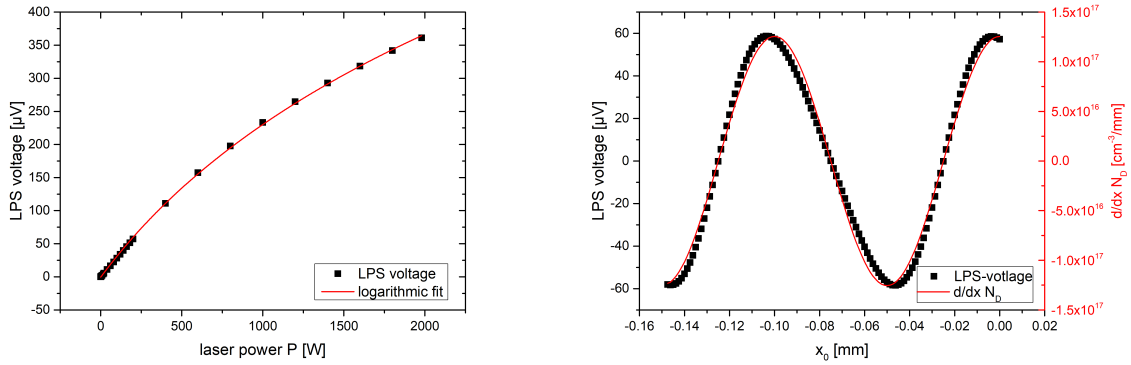

Figure 13: 3D simulation results: LPS voltage as a function of the laser power for $N_{D0} = 1 \times 10^{16}\,\text{cm}^{-3}$ at $(x_0, y_0)^T = (0\,\text{mm}, 0\,\text{mm})^T$ (left) and the LPS voltage as a function of the doping gradient for $N_{D0} = 1 \times 10^{16}\,\text{cm}^{-3}$, $y_0 = 0\,\text{mm}$ and $P = 2\,\text{mW}$ (right).

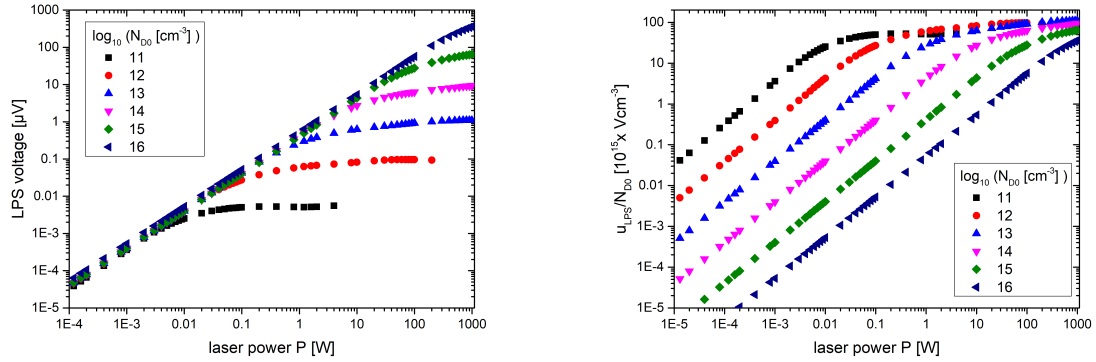

Figure 14: 3D simulation results: LPS voltage as a function of the laser power at $(x_0, y_0)^T = (0\,\text{mm}, 0\,\text{mm})^T$ for various average doping concentrations N_{D0} (left) and ratio of LPS voltage and average doping concentrations as a function of the laser power P for various N_{D0} (right).

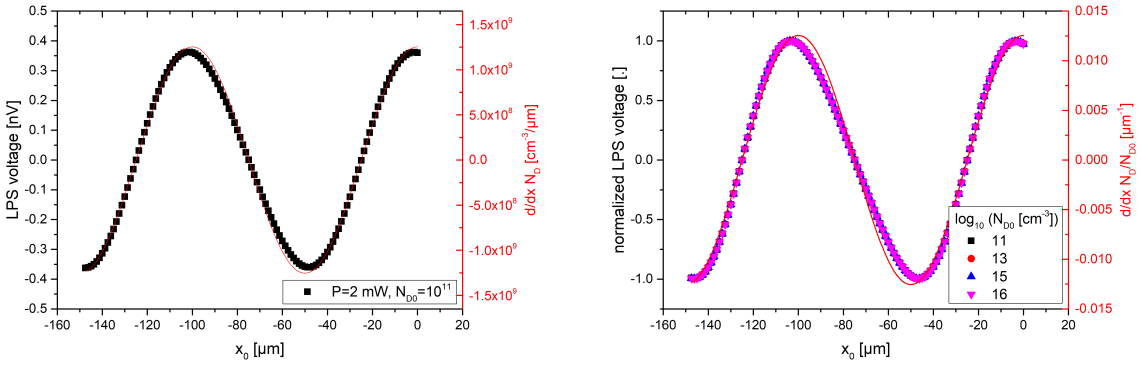

Figure 15: 3D simulation results: LPS voltage scan for $P = 2\,\text{mW}$, $y_0 = 0\,\text{mm}$ and $N_{D0} = 1 \times 10^{11}\,\text{cm}^{-3}$ (left) and normalized LPS voltage scans for $P = 2\,\text{mW}$, $y_0 = 0\,\text{mm}$ and four different base doping levels N_{D0} (right).

for a base doping level of $N_{D0} = 1 \times 10^{11}\,\text{cm}^{-3}$ one needs to be able to detect nanovolts. Up to now, real-life LPS measurement have only been performed for $N_D \geq 1 \times 10^{12}\,\text{cm}^{-3}$. Yet, in practice low doping fluctuations on the order of $N_{D0} = 1 \times 10^{11}\,\text{cm}^{-3}$ do arise, for example, when trying to examine inhomogeneities in the extremely pure Si^{28} crystal which was recently used to redefine the kilogram [1]. Thus, in order to measure these extremely tiny inhomogeneities via the LPS method, our simulations show that one needs to improve the voltage detectors. In Figure 15 left panel, we show an LPS scan for such a very low base doping value $N_{D0} = 1 \times 10^{11}\,\text{cm}^{-3}$. The LPS voltage still follows the doping gradient nearly perfectly. Incidentally, Figure 14 (left panel) also indicates, that measuring highly doped samples ($N_{D0} \geq 1 \times 10^{16}\,\text{cm}^{-3}$) is easier, as the saturation does not limit the measurability up to a laser power of $P = 1000\,\text{W}$.

On the right panel in Figure 14 we show the LPS signal normalized by the base doping level, i.e. u_{LPS}/N_{D0}. For larger laser powers all LPS signals reach the same plateau. Again, this can be explained by the screening effect. It is interesting, that the ratio u_{LPS}/N_{D0} in the plateau regions is nearly independent of the average doping concentration, setting a fundamental barrier for the maximal u_{LPS}/N_{D0} ratio.

Additionally, we performed several LPS scans normalized by the maximal LPS voltage at $x_0 = 0\,\text{mm}$,

that is $u_{max} := u_{LPS}(x_0 = 0)$, for varying N_{D0}, see Figure 15 right panel. It can be seen, that all four normalized scans lie on top of each other. This indicates that

$$\int_{x_0-\delta/2}^{x_0+\delta/2} \frac{1}{N_{D0}} \Delta\sigma(x - x_0)dx \approx \text{const} \tag{41}$$

in (30) as long as the LPS voltages have not saturated yet because in this case u_{max} does not depend on N_{D0} as can be see in Figure 14 (left panel).

5.4 Convergence study

We analyze the convergence order of our method experimentally. Since in practice the LPS voltage u_{LPS} is the quantity of interest, we focus on its relative error with respect to a fine reference solution. Since our doping profiles in the earlier sections only vary in one direction, we run a convergence study in 1D. We choose the doping profile $N_D = N_{D0}\,(1 + 0.2\sin\,(2\pi x/100\,\mu\text{m}))$ on a sequence of nested uniform grids. We fix the number of secant iterations to 20 for every mesh. The reference voltage u_{ref} is computed on a mesh which is two times more refined than the finest mesh used in this study. As can be seen in Figure 16, the LPS voltage converges at first linearly and then approximately quadratically.

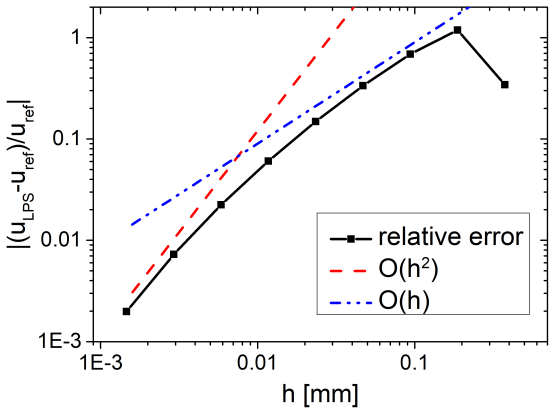

Figure 16: 1D convergence study for $\sigma_L = 20\,\mu\text{m}$, $P = 2\,\text{W}$, $x_0 = 0\,\text{mm}$ and $N_{D0} = 1 \times 10^{16}\,\text{cm}^{-1}$ on a nested sequence of uniform grids.

5.5 Efficiency and comparison

We compare our current implementation with the only other code known to us simulating LPS measurements by Kayser et al. [16, 14] which is based on the commercial COMSOL Multiphysics software package. Unfortunately, it was not possible to run both codes on the same machine due to licencing restrictions. We report that in 1D there were no significant differences. However, for the 3D model in Section 2.6 Table 5.5 shows that even on a computer that is significantly better, the COMSOL implementation computes one LPS voltage nearly 18 times more slowly. Fine tuning of numerical parameters may decrease this gap though we were not able to improve the performance of the COMSOL implementation any further.

	COMSOL	`ddfermi`
system	Windows 10 64-Bit	OpenSuse 15.1 64-Bit
CPU	8x i7-6700 3.4GHz	4x i7-5600 2.6GHz
RAM	32GB	8GB
run time	1516 seconds	85 seconds

Table 1: Comparison of 3D model from Section 5.2 on same anisotropic grid (see Figure 11) run with COMSOL code [14] and our implementation, using three secant iterations. One single LPS voltage is computed for $(x_0, y_0)^T = (0\,\text{mm}, 0\,\text{mm})^T$, N_D chosen as in (40) with $N_{D0} = 1 \times 10^{16}\,\text{cm}^{-3}$ and $P = 1 \times 10^{-19}\,\text{W}$.

Moreover, Kayser showed in his PhD thesis [14], that the commercial COMSOL Multiphysics toolbox can be used to simulate a full LPS scan for the 3D model at the considerably low base doping level $N_{D0} = 1 \times 10^{12}\,\text{cm}^{-3}$. But unfortunately, in this realistic setting the simulation time was on the order of weeks. On the other hand, our implementations were performed on the same OpenSuse notebook from Table 5.5 in approximately two hours. That is, our simulation runs two orders of magnitude faster. This huge speed up is achieved by a clever simulation strategy reusing previously computed results as starting values for the next Newton iteration [11]. It is not exactly clear how the COMSOL Multiphysics toolbox solves the nonlinear system. For base doping levels below $N_{D0} = 1 \times 10^{12}\,\text{cm}^{-3}$ the COMSOL Multiphysics toolbox even failed to produce any results due to numerical instabilities.

6 Conclusion and future research

To improve crystal growth it is paramount to understand the temperature distribution created by the coils. It is impossible to measure the temperature during growth but one can measure inhomogeneities which follow the solid-liquid interface post mortem. We modeled and simulated a special measurement technique of these inhomogeneities, the lateral photovoltage scanning (LPS) since it is fast, cheap and nondestructive. Our model was based on the semiconductor device equations combined with a nonlinear boundary condition, modelling a simple circuit. To validate our 2D and 3D finite volume simulations, we used theory developed by Tauc [22] to prove three analytical predictions, all of which our simulation results satisfied, even for the more complex 2D and 3D settings. Our code runs about two orders of magnitudes faster than earlier implementations based on commercial software. It also performs well for small doping concentrations which previously could not be simulated. We show a quadratic experimental order of convergence on finer meshes. Finally, our simulations provide experimentalists with the lowest reference voltages which their volt meter needs to be able to detect for given doping concentrations. Future research will be concerned with simulating the full inverse problem, requiring a whole new set of techniques.

Acknowledgments

The authors would like to thank Natasha Dropka, Jürgen Fuhrmann, Timo Streckenbach and Hang Si for their valuable input. The temperature field simulation in Figure 1 are courtesy of Robert Menzel (Leibniz-Institut für Kristallzüchtung).

A Model specifications

A.1 Parameter list for silicon

Physical Quantity	Symbol	Value	Units
Reference temperature	T_0	300	K
Electron affinity	$\chi(T_0)$	4.05	eV
Band gap	$E_g(T_0)$	1.12	eV
eff. DOS parameter electrons	κ_n	1.04×10^{19}	$1/\mathrm{cm}^3$
eff. DOS parameter holes	κ_p	2.8×10^{19}	$1/\mathrm{cm}^3$
Density of states in the conduction band	$N_c(T_0)$	1.04×10^{19}	$1/\mathrm{cm}^3$
Density of states in the valence band	$N_v(T_0)$	2.8×10^{19}	$1/\mathrm{cm}^3$
Laser power	P_L	$0 - 20$	mW
Laser wave length	λ_L	685	nm
Laser penetration depth	d_A	4.8	µm
Laser spot radius	σ_L	$\geq$1.25	µm
Direct recombination factor	C_d	1×10^{-20}	cm^3/s
Auger recombination factor electrons	C_n	2.8×10^{-31}	cm^6/s
Auger recombination factor holes	C_p	2.8×10^{-31}	cm^6/s
SRH lifetime electrons	τ_n	$1 \times 10^{-9} - 1 \times 10^{-3}$	s
SRH lifetime holes	τ_p	$1 \times 10^{-9} - 1 \times 10^{-3}$	s
Trap Energy Boron	E_T	0.045	eV
Trap Energy Phosphorus	E_T	0.044	eV
Arora mobility parameter	$\mu^{\mathsf{ref}}_{\mathsf{n},0}$	1323	$\mathrm{cm}^2/\mathrm{Vs}$
Arora mobility parameter	$\mu^{\mathsf{ref}}_{\mathsf{p},0}$	429	$\mathrm{cm}^2/\mathrm{Vs}$
Arora mobility parameter	$\mu^{\mathsf{ref}}_{\mathsf{n},\mathsf{min}}$	89	$\mathrm{cm}^2/\mathrm{Vs}$
Arora mobility parameter	$\mu^{\mathsf{ref}}_{\mathsf{p},\mathsf{min}}$	55	$\mathrm{cm}^2/\mathrm{Vs}$
Arora mobility exponent	α_0	0.88	$-$
Arora mobility exponent	β_1	-0.57	$-$
Arora mobility exponent	β_2	-2.33	$-$
Arora mobility exponent	β_3	2.4	$-$
Arora mobility exponent	β_4	-0.146	$-$

References

[1] *On the revision of the international system of units (SI). Resolution 1 (CGPM 26th meeting, Versailles, November 13–16, 2018)*, Measurement Techniques, 62 (2019), pp. 472–473, https://doi.org/10.1007/s11018-019-01648-4.

[2] G. Alì, A. Bartel, and M. Günther, *Parabolic differential-algebraic models in electrical network design*, Multiscale Modeling & Simulation, 4 (2005), pp. 813–838, https://doi.org/10.1137/040610696.

[3] G. Alì and N. Rotundo, *An existence result for elliptic partial differential–algebraic equations arising in semiconductor modeling*, Nonlinear Analysis: Theory, Methods & Applications, 72 (2010), pp. 4666 – 4681, https://doi.org/10.1016/j.na.2010.02.046.

[4] P. Becker, H. J. Pohl, H. Riemann, and N. Abrosimov, *Enrichment of silicon for a better kilogram*, Physica Status Solidi (A) Applications and Materials Science, 207 (2010), pp. 49–66, https://doi.org/10.1002/pssa.200925148.

[5] M. Burger, H. W. Engl, A. Leitao, and P. A. Markowich, *On inverse problems for semiconductor equations*, Milan Journal of Mathematics, 72 (2004), pp. 273–313, https://doi.org/10.1007/s00032-004-0025-6.

[6] M. Burger, H. W. Engl, P. A. Markowich, and P. Pietra, *Identification of doping profiles in semiconductor devices*, Inverse Problems, 17 (2001), pp. 1765–1795, https://doi.org/10.1088/0266-5611/17/6/315.

[7] K. Cho, M. Numan, T. G. Finstad, W. K. Chu, J. Liu, and J. J. Wortman, *Transient enhanced diffusion during rapid thermal annealing of boron implanted silicon*, Applied Physics Letters, 47 (1985), pp. 1321–1323, https://doi.org/10.1063/1.96267.

[8] D. H. Doan, P. Farrell, J. Fuhrmann, M. Kantner, T. Koprucki, and N. Rotundo, *ddfermi – a drift-diffusion simulation tool*, version: 0.1.0, Weierstrass Institute (WIAS), doi: http://doi.org/10.20347/WIAS.SOFTWARE.14, 2018.

[9] R. Eymard, T. Gallouët, and R. Herbin, *Finite volume methods*, in Solution of Equation in $\mathbb{R}^n$ (Part 3), Techniques of Scientific Computing (Part 3), vol. 7 of Handbook of Numerical Analysis, Elsevier, 2000, pp. 713 – 1018.

[10] P. Farrell, T. Koprucki, and J. Fuhrmann, *Computational and analytical comparison of flux discretizations for the semiconductor device equations beyond boltzmann statistics*, Journal of Computational Physics, 346 (2017), pp. 497–513, https://doi.org/10.1016/j.jcp.2017.06.023.

[11] P. Farrell, N. Rotundo, D. Doan, M. Kantner, J. Fuhrmann, and T. Koprucki, *Mathematical methods: Drift-diffusion models*, in Handbook of Optoelectronic Device Modeling and Simulation, J. Piprek, ed., vol. 2, CRC Press, 2017, ch. 50, pp. 733–771.

[12] H. Gajewski, *Analysis und Numerik von Ladungstransport in Halbleitern*, WIAS Report, 0 (1993). ISSN 0942-9077.

[13] K. Gärtner, *Existence of bounded discrete steady-state solutions of the van roosbroeck system on boundary conforming delaunay grids*, SIAM Journal on Scientific Computing, 31 (2009), pp. 1347–1362, https://doi.org/10.1137/070710950.

[14] S. Kayser, *The lateral photovoltage scanning method to probe spatial inhomogeneities in semiconductors: a joined numerical and experimental investigation*, PhD thesis, Brandenburg University of Technology, Expected 2020.

[15] S. Kayser, P. Farrell, and N. Rotundo, *Detecting striations via the lateral photovoltage scanning method without screening effect*, WIAS Preprint 2785, (2020).

[16] S. KAYSER, A. LÜDGE, AND K. BÖTTCHER, *Computational simulation of the lateral photovoltage scanning method*, In Proceedings of the 8th International Scientific Colloquium, (2018), pp. 149–154.

[17] T. KOPRUCKI, N. ROTUNDO, P. FARRELL, D. H. DOAN, AND J. FUHRMANN, *On thermodynamic consistency of a Scharfetter-Gummel scheme based on a modified thermal voltage for drift-diffusion equations with diffusion enhancement*, Optical and Quantum Electronics, 47 (2015), pp. 1327–1332, https://doi.org/10.1007/s11082-014-0050-9.

[18] A. LEITAO, P. MARKOWICH, AND J. ZUBELLI, *On inverse doping profile problems for the stationary voltage–current map*, Inverse Problems, 22 (2006), pp. 1071–1088, https://doi.org/10.1088/0266-5611/22/3/021.

[19] A. LÜDGE AND H. RIEMANN, *Doping Inhomogeneities in Silicon Crystals Detected by the Lateral Photovoltage Scanning (LPS) Method*, Inst. Phys. Conf. Ser., 160 (1997), pp. 145–148.

[20] D. SCHARFETTER AND H. GUMMEL, *Large-signal analysis of a silicon read diode oscillator*, IEEE Transactions on Electron Devices, 16 (1969), pp. 64–77, https://doi.org/10.1109/T-ED.1969.16566.

[21] S. SELBERHERR, *Analysis and simulation of semiconductor devices*, Springer, Wien, New York, 1984.

[22] J. TAUC, *The Theory of a Bulk Photo-Voltaic Phenomenon in Semi-Conductors*, Institute of technical Physics, Czechosl., 5 (1955), pp. 178–191.

[23] L. VALDES, *Resistivity Measurements on Germanium for Transistor*, Proceeding of the I.R.E, 42 (1954), pp. 420–427, https://doi.org/10.1109/JRPROC.1954.274680.

[24] W. ZULEHNER, *The growth of highly pure silicon crystals*, Metrologia, 31 (1994), pp. 255–261, https://doi.org/10.1088/0026-1394/31/3/012.